Available online at www.sciencedirect.com
SCIENCE DIRECT®
Mechanism and Machine Theory 40 (2005) 1345–1366
Mechanism and Machine Theory
www.elsevier.com/locate/mechmt

Design of a high-impact survivable robot

D. O'Halloran, A. Wolf *, H. Choset

Biorobotics Lab, Department of Mechanical Engineering and the Robotics Institute, Carnegie Mellon University, Newell-Simon Hall, 5000 Forbes AV, Pittsburgh, PA 15213, USA

Received 12 April 2004; received in revised form 12 December 2004; accepted 11 February 2005
Available online 7 April 2005

Abstract

This paper presents the design, construction, and testing of a two-wheeled low-cost mobile robot platform that has high survivability when subjected to large impact forces and general rough handling. The design of the drive transmission system and integrated suspension system is developed, along with general equations of motion describing their dynamics. Analyses were conducted to insure stability of the various subsystems and optimize parameters for the desired vibration characteristics. Equations of motion were also developed to describe the rocking chassis phenomenon inherent to the two-wheeled design. A flywheel compensation scheme which helps eliminate the rocking chassis problem is also outlined. An impact analysis combining theory and empirical data was used to predict the survivability threshold. Finally, three series of experiments were conducted, with the first two followed by design improvements. In contrast to currently available commercial robots, our new design employs a flexible mechanical platform capable of absorbing energy during high load impacts. This design was substantiated during the final tests when the robot survived a third story drop without any damage.

Keywords: Two wheel robot; Survivable robot; Robot design

* Corresponding author. Tel.: +1 412 578 5368.
E-mail addresses: dmo@andrew.cmu.edu (D. O'Halloran), alon.wolf@cmu.edu (A. Wolf), choset@cs.cmu.edu (H. Choset).

0094-114X/$ - see front matter © 2005 Elsevier Ltd. All rights reserved.
doi:10.1016/j.mechmachtheory.2005.02.004

Nomenclature

W	component weight
m	component mass
S	spring force
k	spring constant
d	spring displacement
N	normal force or bearing force
T	tension in drive belt
L	belt section length
r	component radius
θ	angle between components
H	tire bearing force
C	spring collar bearing force
B	chassis bearing force
M	moment or torque
A	motor reaction force
Θ_C	angle of chassis with respect to vertical axis
Q	countering force provided by some balancing system (such as flywheel)
M_Q	countering moment provided by some balancing system
I	moment of inertia
α	angular acceleration
$a_{C,y}$	linear acceleration of chassis in y-direction

Subscripts

X	In x-direction
Y	In y-direction
P	pulley
S	spring
i	idler
C	chassis

1. Introduction

Urban search and rescue (USAR) robots have recently become much more widely accepted as a vital field tool in emergency situations. Recent past events such as the Mexico City earthquake in 1985, the 1995 Oklahoma City bombing, and the September 11 attack on the World Trade Center have shown that dangerous and inaccessible regions are major problems during a rescue operation. In Mexico City earthquake, 135 rescue workers were killed, 65 of the 135 died while trying to search and rescue while going through confined spaces which were flooded trapping the rescue workers inside [1,2]. The roles of robots also continue to expand in military reconnaissance missions, such as in the search for terrorist cells hidden deep inside caves in Afghanistan during 2001–

2002. However, the effectiveness of current robot designs in these environments is limited by numerous factors. One such factor is the inherent fragility of many of the current robots, which makes these robots susceptible to failure due to rough handling or impacts which occur during these missions. This paper presents a design for a mobile robot platform that improves the robots survivability when subjected to high impact forces and general rough handling, is compact, and can fulfill the role of a search and rescue or reconnaissance aid robot.

A limited amount of previous work has been done on researching the primary factors which contribute to robot survivability. Cameron and Arkin [3] studied the survival rate and behavior of falling cats to better understand the characteristics that allow these animals to survive falls of great height so that they might formulate a set of criteria that should be satisfied for robots to survive similar falls. Two of their conclusions of interest are that the robot must be able to situate itself in a manner in which its locomotion actuators (wheels, legs, etc.) impact the ground first, and secondly that compliance is necessary to absorb the energy of impact. In other research Arkin [4] describes various ways control and redunancy can be used to increase the fault tolerance of a robot under harsh operating conditions.

In actual practical application, two other key robots have been deployed for similar missions and are touted for their impact survivability. The PackBot, developed by the iRobot Corporation [5], is a tracked robot with a small main chassis profile. Product specifications claim that the robot is capable of surviving a fall from up to 2 m onto concrete, as well as tumbling down stairs. The robot has a height of only about 8 in. and weighs in approximately 50 lbs. This robot has seen extensive real-world field deployment at both the WTC disaster site and during military missions in Afghanistan. The second robot for comparison is the Dragon Runner developed at the National Robotics Engineering Consortium at Carnegie Mellon University [6]. Dragon Runner weighs about 16 pounds and has four large wheels which extend above and below the base chassis profile. While this robot is still in development, in its current form the designers claim it to be able to survive impacts at full speed or from a third story drop. These two robots will be used as baselines for comparison to evaluate the performance of the new robot design outlined within this paper, with our goal to build a robot capable of surviving a third story drop but at costing a magnitude less than these two designs.

The work presented here specifically details the mechanical design of the general robot configuration and its drive system. A rudimentary remote control system was used to control the robot during experiments, though the robot is made to accommodate more sophisticated control electronics at a later phase. Additionally, the mechanical design incorporates measures to minimize the shock loads that would be transmitted to the current and possible future electronic components.

This paper is organized as follows: Section 2 presents an overview of the general robot configuration used for the design, including a discussion of the advantages and limitations of this configuration. Section 3 details the conceptual design of the transmission system while Section 4 covers the development of the unique suspension system. Section 5 will address in detail the general motion limitations of the robot configuration and the proposed compensation scheme. Section 6 details theoretical predictions for the impact capability of the design, while Section 7 discusses the actual experimental drop tests and the subsequent design improvements. Finally, the conclusions of this robot design and experimentation project are covered in Section 8.

2. General configuration

One of the first general design decisions that had to be made was the locomotion scheme for the robot. Each of the standard locomotion choices, legged, wheeled, and tracked, have their advantages and disadvantages. However, given the primary goal of this robot to survive impacts, wheeled locomotion is the best choice. It offers reasonably good traction on most terrains and more importantly has the best shock absorption capability of the three choices mentioned above due to the intrinsic elasticity of most tires. More specifically this design will utilize pneumatic tires due to their superior shock absorption capabilities.

The primary metric used in evaluating each of the robot design choices was that the robot must be capable of withstanding a fall from at least 9.1 m, so as to equal or improve upon the performance of the best commercially available platforms. The reason for desiring a robot that can withstand such falls is that is it is conceivable that a robot acting in a search and rescue or military reconnaissance capacity might inadvertently or even intentionally be driven off a ledge. Considering the potential for such an event adds a significant complicating factor in designing an impact-survival mechanical platform.

In general the orientation of the robot upon impact with the ground cannot be known with any certainty; therefore the robot must be protected from impact in all directions. Even if the assumption is made that lateral disturbances acting on the robot during its fall are negligible enough that the robot will not topple about an axes orthogonal to the drive axles, the propensity for the robot to spin about an axes parallel to the drive axles will still exist, meaning the robot could land in an orientation upside down from its usual driving state. Therefore the general configuration must at a minimum provide protection against impact in all directions orthogonal to the drive axles.

Given that pneumatic tires are being used as a first line of defense against impact, it makes sense to design the robot so that the tires will be the first component to contact the ground regardless of robot orientation. To this end, the robot chassis has been designed so that it fits entirely within the outer profile of the tires as seen in Fig. 1. A four wheeled robot could fulfill this criterion; however, this design carries with it several disadvantages. First, while a differential drive could in theory be used for steering it would not be as efficient as on a two wheeled robot due to the extra friction forces created by the extra two tires. Second, if the more typical and efficient rack-and-pinion steering scheme were used for a four wheeled robot, this would add components and

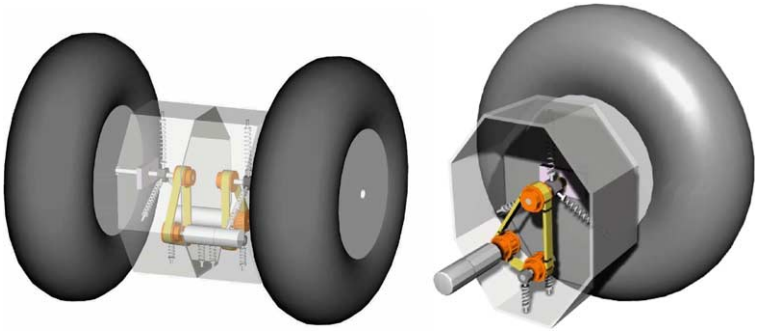

Fig. 1. Two-wheel suspended chassis configuration.

complexity to the overall robot which would therefore increase the number of failure points. Also, in a four wheeled scheme the section of chassis extending between the two wheels is laterally unprotected and could potentially be impacted by obstacles which fit between the wheels. Finally, the extra two wheels add size and mass to the overall robot leading to higher impact forces and decreasing the robot's portability. Due to these limitations, this design employs a two wheeled driving scheme, shown in Fig. 1 which does not suffer from the above mentioned problems.

Alas, a two wheeled robot has limitations of its own. In a four wheeled robot when the motors drive two of the wheels, the other two wheels provide a reaction force with the ground which prevents the chassis from spinning about the drive axle as opposed to the wheels. Other robots have employed this two wheel scheme, though none strictly in the manner of this robot. The nBot balancing robot developed by Anderson actually carries its chassis above its drive shafts like an inverted pendulum, thus having active control of the balance in the absence of any structure to provide a reaction force [7]. Most conventional two-wheeled robots, such as those often used by hobbyist or research robots such as the Nomad Scout always have an inert third caster wheel or dragging structural piece which provides the reaction force and maintains the balance of the robot. However, in this design there is no component extending beyond the wheel profile to provide a ground reaction force. Therefore, when the motors apply torque to the drive shafts there will be a battle between the chassis and the wheels to see which one actually rotates. This means that for accelerations beyond a certain threshold the chassis will spin rather than the wheels. This phenomenon along with a compensation scheme will be more fully detailed and explored in Section 5.

3. Drive transmission design

A number of power transmission options were examined in order to determine the optimal transmission scheme for this robot design. The main criteria in evaluating these different options were the transmissions' capability of minimizing the shock and vibration transmitted to the motors, simplicity of the system which translates to minimizing potential failure points, and mechanical efficiency of the system.

The first option, a spur gear transmission has the advantages of simplicity and minimal component count, as well as high mechanical efficiency [8]. A bevel gear transmission is similarly simple though slightly less efficient than a spur gear transmission. It does however allow the motors to be mounted vertically which helps to minimize the width of the chassis and henceforth the overall robot size. A worm gear transmission would also allow for the motors to be mounted vertically and offers high gear ratios, though they are expensive and relatively inefficient. All three of these geared transmissions suffer from a similar major disadvantage in that they are poor at absorbing shock. Another option is a chain drive transmission. A chain drive provides flexibility in the placement of the motors so as to minimize the overall chassis size, has better shock absorption capabilities than gear transmissions, and still has high efficiency. However, a chain drive requires lubrication for smooth operation and contains numerous links which each represent additional failure points. The final option is a belt drive transmission. This system has the same flexibility of motor placement as the chain drive and better shock absorption capabilities due to the inherent elasticity of timing belts. Additionally this system is efficient, quiet, and requires no lubrication.

Therefore, the belt drive system was chosen as the initial transmission scheme based on the evaluation criteria.

4. Suspension design

The flexible nature of the belt drive system allowed us to include a unique suspension system shown in Fig. 2, which would further enhance the overall shock absorption capability of the transmission. In order to discuss the details of this suspension, we shall first define a fixed coordinate system whose z-axis points from the wheel towards the chassis and whose y-axis points upward with respect to the ground. The drive shaft connected to the wheel is mounted to the chassis via a spherical bearing which allows the shaft limited rotation (10° off of perpendicular axis) about the x and y axes, in addition to the typical z-axis rotation that allows transmission of torque to the wheels. A pulley (p2) is mounted at the end of the shaft internal to the chassis. The timing belt wraps around pulley p2, a pulley (p1) attached to a drive motor mounted to the chassis, and a free spinning idler pulley (p3). The idler pulley is attached to a shaft connected to a pair of springs which allow the pulley to move in order to compensate for motion of pulley p2, thus preserving the overall length of the belt and the tension in the belt that allows for the transmission of torque. Three suspension springs attached at opposite ends to the chassis and to a free spinning shaft collar provide the centering force which keeps the shaft horizontal under static conditions. We also considered substituting a membrane for the three springs. A membrane would have easily added dampening to the system [9]. However, due to the configuration of the system the membrane would need to have non-axisymmetrical properties which would not be easily achieved.

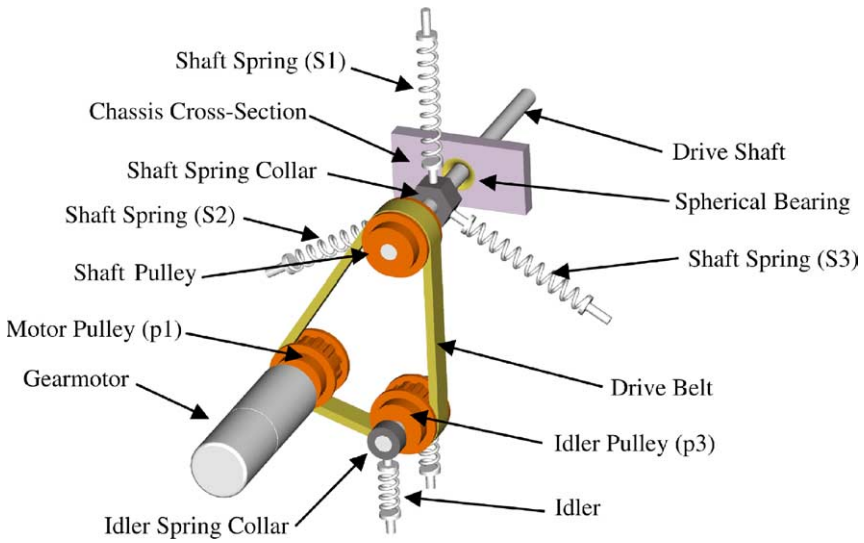

Fig. 2. Belt transmission/chassis suspension.

4.1. General suspension equations

In order to analyze and optimize the detail design of the suspension system, general equations of motion (EOM) were developed for each component of the system. In total 37 equations are needed to describe the general motion of the suspension system.

One of the key components in the system is the drive shaft, shown in Figs. 3–5, since it is directly responsible for translating torques out to the wheel from the motor and for back propagating the motion from the wheel caused by an impact. The particular equations for the shaft are shown below, where the force balance in the x-direction is given by Eq. (1), the y-direction Eq. (2), the moment balance about the z-axis Eq. (3), about the y-axis Eq. (4) and about the x-axis Eq. (5), with all three moment equations passing through the shaft center of gravity (see Nomenclature).

$$N_{p2,x} + C_x - B_x - H_x - W_S \sin\theta_C = m_S \ddot{x}_S \tag{1}$$

$$H_y - N_{p2,y} + C_y - B_y - W_S \cos\theta_C = m_S \ddot{y}_S \tag{2}$$

$$M_S - M_W = I_{S,z}\alpha_{s,z} \tag{3}$$

$$1/2C_x(L_1 + L_2 - L_3) - 1/2N_{p2,x}(L_1 + L_2 + L_3) - 1/2B_x(L_2 + L_3 - L_1) + 1/2H_x(L_1 + L_2 + L_3) = I_{S,y}\alpha_{s,y} \tag{4}$$

$$1/2N_{p2,y}(L_1 + L_2 + L_3) - 1/2C_y(L_1 + L_2 - L_3) - 1/2B_y(L_2 + L_3 - L_1) + 1/2H_y(L_1 + L_2 + L_3) = I_{S,x}\alpha_{s,x} \tag{5}$$

The other key component in analyzing the behavior of the suspension system is the chassis shown in Figs. 6 and 7, since this component ties the shaft, drive system, and suspension system together. The EOM for this part are presented below. Note that the moment equation is taken with respect to the drive shaft axis.

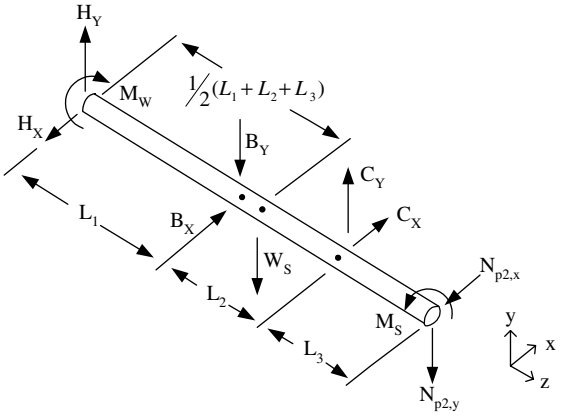

Fig. 3. Drive shaft free body diagram.

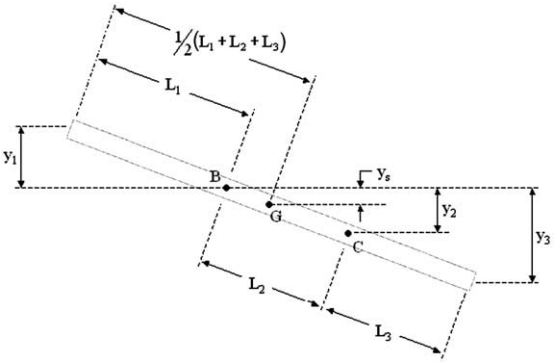

Fig. 4. Drive shaft deflection geometry.

Fig. 5. CAD model of shaft system.

$$S_{R,2}\sin\theta_{R,S2-d} - S_{R,3}\sin\theta_{R,S3-d} - S_{L,2}\sin\theta_{L,S2-d} + S_{L,3}\sin\theta_{L,S3-d} - B_{R,x} + B_{L,x} - A_{L,x} + A_{R,x} + Q_x - W_C\sin\theta_C = m_C a_{C,x} \tag{6}$$

$$S_{R,2}\cos\theta_{R,S2-d} + S_{R,3}\cos\theta_{R,S3-d} - S_{R,1} + S_{L,2}\cos\theta_{L,S2-d} + S_{L,3}\cos\theta_{L,S3-d} - S_{L,1} + B_{R,y} + B_{L,y} + 2S_{L,i} + 2S_{R,i} - W_C\cos\theta_C + A_{L,y} + A_{R,y} - Q_y = m_C a_{C,y} \tag{7}$$

$$S_{R,2}d_{s,y}\sin\theta_{R,S2-d} - S_{R,3}d_{s,y}\sin\theta_{R,S3-d} - S_{R,2}d_{c,w}\cos\theta_{R,S2-d} + S_{R,3}d_{c,w}\cos\theta_{R,S3-d} - S_{L,2}d_{s,y}\sin\theta_{L,S2-d} + S_{L,3}d_{s,y}\sin\theta_{L,S3-d} + S_{L,2}d_{c,w}\cos\theta_{L,S2-d} - S_{L,3}d_{c,w}\cos\theta_{L,S3-d} - S_{R,1}d_{c,h}\sin\theta_{R,S1-d} + S_{L,1}d_{c,h}\sin\theta_{L,S1-d} + A_{R,x}d_{A,y} - A_{L,x}d_{A,y} - A_{R,y}d_{A,x} + A_{L,y}d_{A,x} - M_{R,A} - M_{L,A} + Q_x d_Q = I_{C,z}\alpha_C + m_C(d_{gc}\alpha_C)d_{gc} \tag{8}$$

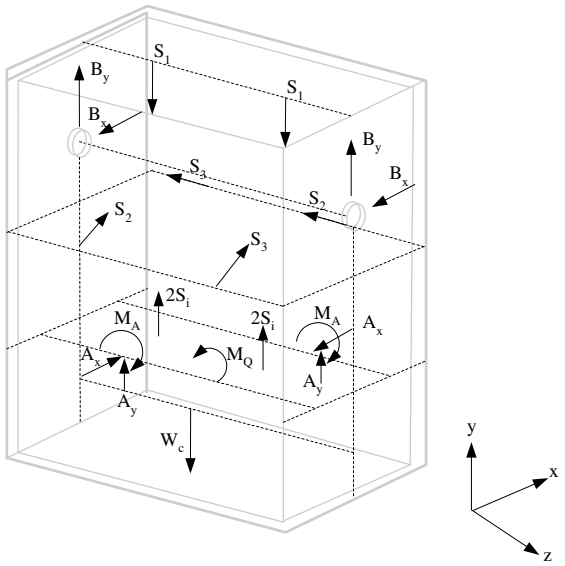

Fig. 6. Three dimensional chassis free body diagram.

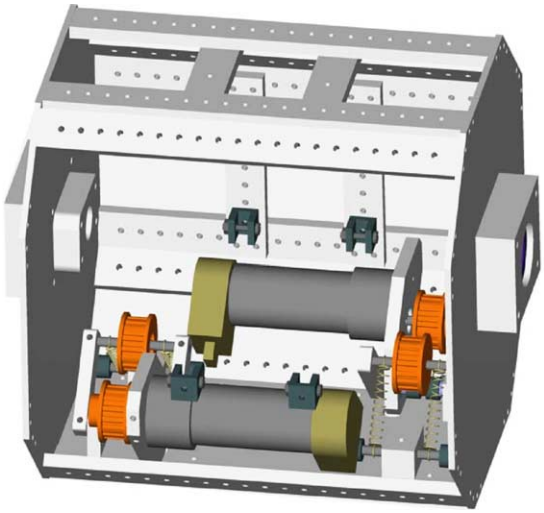

Fig. 7. CAD model of chassis.

With the general equations of motion derived, static equilibrium conditions can now be solved for; giving the starting point for developing the detailed configuration and design of the robot's various components.

4.2. Static analysis and optimization

Given the general equations of motion shown above, the next step in the design process was to solve for the various parameters under static conditions. Obviously since this is a static analysis all

the bodies are at rest. Given static equilibrium conditions, the tension in the belt should therefore be uniform [10]. All weights, masses, lengths, and angles are known parameters.

Using these assumptions along with various substitutions and algebraic manipulations of the general EOM derived above yields 22 static specific EOM. However, we are left with 24 unknowns. Contrary to what this might first indicate, the system is in fact not statically indeterminate. The reason being that some of the parameters, namely the spring forces, can be independently controlled since they depend solely on spring constants and deflection, two parameters which can be chosen at will for each spring. The consequence of this result is that two of the spring forces become design parameters. In order to best control the performance of the overall system we pick spring forces from two different subsystems as the design parameters, namely the idler spring (Si) and the vertical suspension spring (S1).

With the design parameters specified it is then possible to solve for all unknowns. While all the parameters are useful in evaluating maximum stresses in the various components, the spring forces (S_1, S_2, S_3, S_i) are of particular interest since they most directly will affect the suspension performance. The resulting equations, Eq. (9), and Eq. (10) for the dependent spring forces (S_2, S_3) are shown below in terms of only known parameters.

$$\begin{aligned} S_2 = {} & \left[S_1 - \left(\left(\frac{2(S_i + W_{i,SC}) + W_{i,S} + W_{p3}}{\sin\theta_{p2} + \cos\theta_{p3}} \right) (\sin\theta_{p1} + \cos\theta_{p3}) + W_{p2} \right) \left(\frac{L_1 + 2L_3 + L_2}{L_2} \right) \right. \\ & - \frac{L_1}{L_2} \left(\left(\frac{2(S_i + W_{i,SC}) + W_{i,S} + W_{p3}}{\sin\theta_{p2} + \cos\theta_{p3}} (\sin\theta_{p1} - \sin\theta_{p2}) - W_{p1} \right) - 2S_i + \frac{1}{2} W_C + W_{SC} \right) \\ & \left. - \frac{L_3}{L_2} (W_S) - \left(W_{SC} - \left(\frac{2(S_i + W_{i,SC}) + W_{i,S} + W_{p3}}{\sin\theta_{p2} + \cos\theta_{p3}} \right) \frac{(\cos\theta_{p1} + \sin\theta_{p3})(L_3 + L_2)}{L_2} \cot\theta_{S3} \right) \right] \\ & \times \frac{\sin\theta_{S3}}{\sin(\theta_{S2} + \theta_{S3})} \end{aligned} \tag{9}$$

$$S_3 = \left[S_2 \sin\theta_{S2} - \left(\frac{2(S_i + W_{i,SC}) + W_{i,S} + W_{p3}}{\sin\theta_{p2} + \cos\theta_{p3}} \right) (\cos\theta_{p1} + \sin\theta_{p3}) \left(\frac{L_3 + L_2}{L_2} \right) \right] \frac{1}{\sin\theta_{S3}} \tag{10}$$

For maximum stability all springs should always remain in tension since a compressive state is inherently unstable. An analysis of a general range of values for the design spring parameters (S_1, S_i) gives the design space for which the dependent springs (S2, S3) remain in tension as shown in Figs. 8 and 9.

Using these graphs, we can insure that our choices of spring values for S1 and Si result in a tensile state for S2 and S3 by checking that the corresponding point on the functional plane is above zero on the z-axis.

4.3. Displacement analysis

Once the static parameters are known, the general motion of the suspension system, given some initial conditions or forcing functions, can be solved. This general disturbance analysis can also be used as a first approximation of the system reaction to impact.

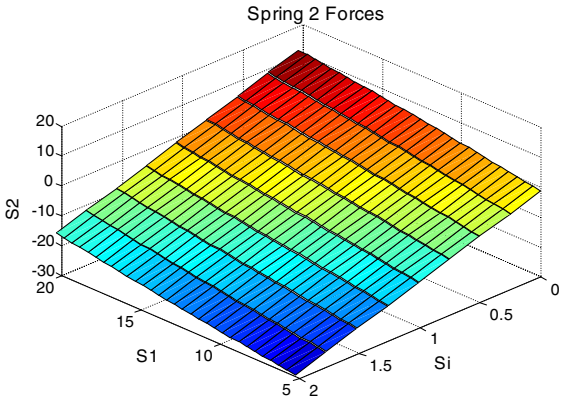

Fig. 8. Spring S2 force as a function of S1 and Si (all in lbs).

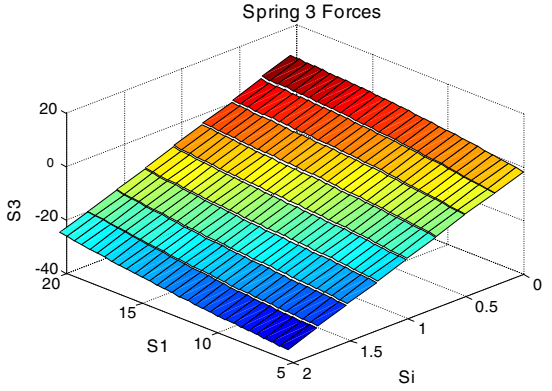

Fig. 9. Spring S3 force as a function of S1 and Si (all in lbs).

In either an impact study or a general disturbance analysis it is reasonable to assume that the disturbance acts in only one radial direction since the tire theoretically makes line contact with the ground. Therefore, to simplify the analysis we will assume the disturbance acts in only a y-direction. However, it should be noted that this disturbance in one direction may cause motion in both the y and x directions due to the configuration of the suspension system. Also to further simplify the geometry of the problem we will conduct the analysis with the chassis held stationary while the suspension system and the tire are free to move, while a equivalent ground force is applied to the tire in order to maintain initial static equilibrium. If we were instead to let all bodies move relative to a fixed ground we would end up with additional time dependent terms to locate the point on the drive shaft which has zero displacement, thus complicating the equations. Using the stationary chassis approach let us mandate that the point on the shaft passing through the spherical bearing of the chassis is always the point of zero displacement. This then allows us to easily relate all displacements back to the general displacement of the tire end of the shaft.

For this analysis a more complete set of equations is needed to describe the elasticity of the tire and its influence on the overall suspension system. Modeling the tire as a simple spring

(dampening will later be added to the model) as shown in Fig. 10 yields the following equation for the normal force acting on the wheel hub.

$$N_w = k_T(y_0 - y_g(t) + y_1(t)) \tag{11}$$

In order to complete this analysis a number of geometric relationships must be developed (Fig. 11). The first relationship is that of the suspension spring displacements to the general shaft displacement as illustrated in Fig. 12. Based on this diagram, the general spring displacements are given by Eqs. (12)–(14).

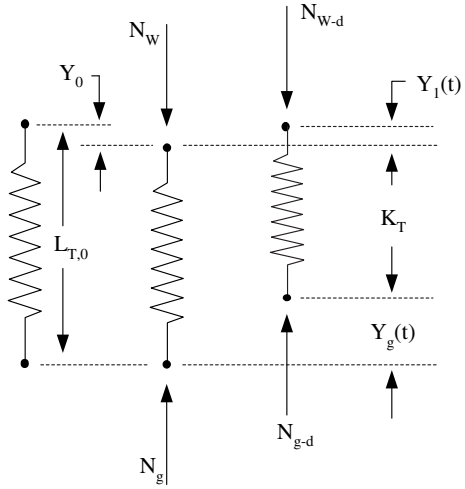

Fig. 10. Tire spring model.

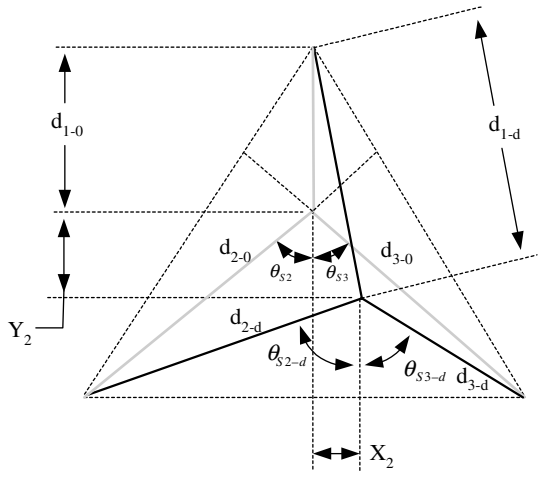

Fig. 11. General spring displacement geometry.

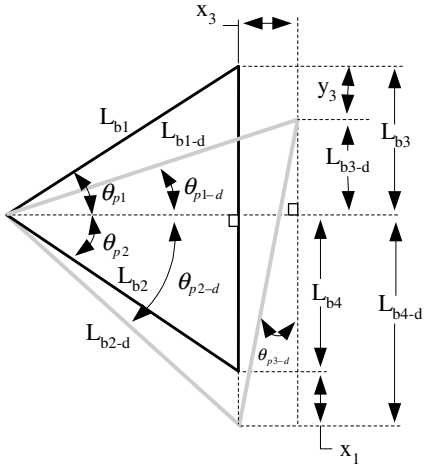

Fig. 12. General belt deflection geometry.

$$d_{1-\mathrm{d}} = \sqrt{\left(d_{1-0} + y_1\left(\frac{L_2}{L_1}\right)\right)^2 + \left(x_1\left(\frac{L_2}{L_1}\right)\right)^2} \tag{12}$$

$$d_{2-\mathrm{d}} = \sqrt{\left(d_{2-0}\cos\theta_{\mathrm{S2}} - y_1\left(\frac{L_2}{L_1}\right)\right)^2 + \left(d_{2-0}\sin\theta_{\mathrm{S2}} + x_1\left(\frac{L_2}{L_1}\right)\right)^2} \tag{13}$$

$$d_{3-\mathrm{d}} = \sqrt{\left(d_{3-0}\cos\theta_{\mathrm{S3}} - y_1\left(\frac{L_2}{L_1}\right)\right)^2 + \left(d_{3-0}\sin\theta_{\mathrm{S3}} - x_1\left(\frac{L_2}{L_1}\right)\right)^2} \tag{14}$$

Another geometric relationship that must be developed is the motion of the idler spring and the overall profile of the transmission belt as a function of shaft displacement. The key to this relationship is that the overall belt length must remain constant. As both a design and analysis simplification all three pulleys are chosen to have the same radius. Given this simplification, the total amount of belt wrapped around all three pulleys will always be equal to the circumference of one pulley. Therefore, the analysis can be simplified to analyzing simply the changing distances between pulley centers as illustrated by a deforming triangle as shown in Fig. 13. This yields the following five equations which can be combined to find a general equation for the idler pulley displacement, though that exact result is too lengthy to include here.

$$L_{\mathrm{b3-d}} = L_{\mathrm{b3}} - y_3 \tag{15}$$

$$L_{\mathrm{b4-d}} = L_{\mathrm{b4}} + y_{\mathrm{i}} \tag{16}$$

$$L_{\mathrm{b1-d}} = \sqrt{(L_{\mathrm{b1}})^2 - (L_{\mathrm{b3}})^2 + 2\cdot x_3\sqrt{(L_{\mathrm{b1}})^2 + (L_{\mathrm{b3}})^2} + (x_3)^2 + (L_{\mathrm{b3}} - y_3)^2} \tag{17}$$

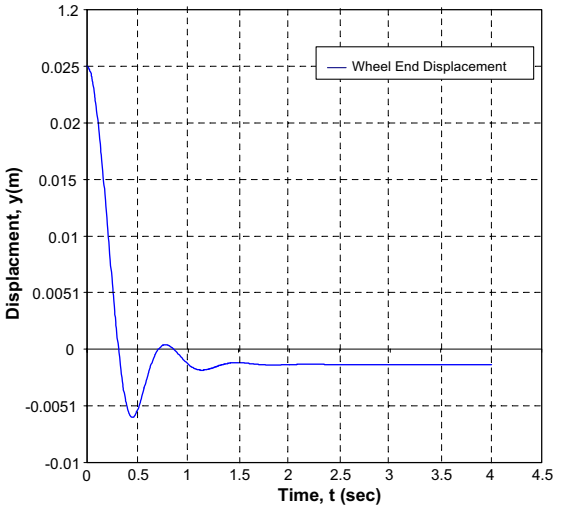

Fig. 13. 1-DOF suspension performance.

$$L_{b2-d} = \sqrt{(L_{b1})^2 - (L_{b3})^2 + (L_{b4} + y_i)^2} \tag{18}$$

$$L_{b1} + L_{b2} + L_{b3} + L_{b4} = L_{b1-d} + L_{b2-d} + \sqrt{(L_{b3-d} + L_{b4-d})^2 + (y_i)^2} \tag{19}$$

With these relationships derived, it is then possible to produce three coupled differential equations, Eq. (20)–(22), describing the system. The overall system can therefore be characterized as a 3 degree-of-freedom (DOF) vibration problem. It should be noted that the actual complexity of these equations is not fully illustrated here since some of the parameters are actually functions of the displacements and their derivatives and have not been fully expanded for the sake of compactness in the presentation of these equations.

$$\begin{aligned} &4L_1(L_1 + L_2)(k_T(y_0 - y_g(t) + y_1(t)) - W_w - m_w\ddot{y}_1) \\ &\quad = 2I_{S,x}\ddot{y}_1(L_1 + L_2 + L_3) - m_S\ddot{y}_1(L_1 - L_2 - L_3)(L_1 + L_2 - L_3) \\ &\qquad + 2L_1(2B_yL_2 + W_S(L_1 + L_2 - L_3) - 2N_{p2,y}L_3) \end{aligned} \tag{20}$$

$$\begin{aligned} 4L_1(L_1 + L_2)m_w\ddot{x}_1 = {} & 2I_{S,y}\ddot{x}_1L_1(L_1 + L_2 + L_3) + m_S\ddot{x}_1(L_1 - L_2 - L_3)(L_1 + L_2 - L_3) \\ & - 4B_xL_1 + 4L_1N_{p2,x}(L_1 + L_2) \end{aligned} \tag{21}$$

$$\ddot{y}_1(t) = -\ddot{y}_g(t) \tag{22}$$

We then reduced the problem to a 1-DOF vibration problem to get a first approximation of the behavior of the system. To this end we will assume all displacement in the suspension system acts in the y-direction. Next, by removing the spring we will look at the displacement of the shaft independent of the tire. Lastly, we will make a geometrical assumption that the displacement of the idler pulley (P3) is equal to the displacement of the shaft pulley (P2). Given

these assumptions we end up with a new governing differential equation as shown below. Again it should be noted that the true complexity of this equation is masked by the fact that substitutions have not yet been made for several parameters which in fact depend on the displacement and its derivatives.

$$4(L_1)^2(N_w - W_w - m_w\ddot{y}_1) = -2L_1 I_{S,x}\ddot{y}_1(L_1 + L_2 + L_3) + m_S\ddot{y}_1(-L_1 + L_2 + L_3)^2 + 2L_1(-2C_yL_2 + W_S(-L_1 + L_2 + L_3) + 2N_{p2,y}L_1) \quad (23)$$

Dampening can be added to the system via the C_y parameter as this directly corresponds to the spring suspension system. A numerical solution can then be found for this 1-DOF differential equation. With the dampening added, it can be shown that this system is in fact stable as shown by the plot of Fig. 13 of the numerical solution of the shaft displacement generated by a Runga Kutta method.

Future analyses will be aimed at optimizing the spring and dampening parameters to achieve the smoothest and most well-behaved suspension system performance, as well as incorporating the other two DOF of the system into the vibration analysis.

5. General chassis motion

As discussed briefly in Section 2, the two wheeled configuration of the robot presents the challenge of balancing the unwanted motion of the chassis against the desired motion of the wheels. When the motor begins to exert a torque on the drive pulley, there must be a balancing moment at the connection with the chassis to keep the motor from spinning. In the absence of an additional ground contact point to provide a reaction force, this moment will have the effect of causing the chassis to rotate about the drive shaft. However, assuming the mass center is located below this pivot point, as the chassis rotates the gravitational forces will begin to create a countering moment. Assuming the accelerations are small enough at some point the moment will no longer be able to rotate the chassis and instead the rotational inertia of the wheels will be overcome causing them to start rotating, or in other words for the torque to be transmitted to the desired location. This cyclical motion is described by the differential equation of the chassis angle with respect to time shown below.

$$\left(\frac{M_w - H_x\cos\theta_C + H_y\cos\theta_C}{I_w + m_T(r_w)^2}\right) r_W\cos\theta_C(2m_m - m_C) + \ddot{\theta}_C\left(2m_m\sqrt{(d_{A,x})^2 + (d_{A,y})^2} - m_C d_{gc}\right) - W_C\sin\theta_C = 0 \quad (24)$$

The numerical solution for this equation illustrates the rocking motion of the chassis for small accelerations (Fig. 14). This analysis also shows that above a threshold dependent on the chassis weight distribution the chassis will simply spin while the wheels will remain stationary. Therefore, if we hope to reduce the acceleration limitations of this design we must implement some system for countering chassis rocking motion. One such system is detailed in the following subsection.

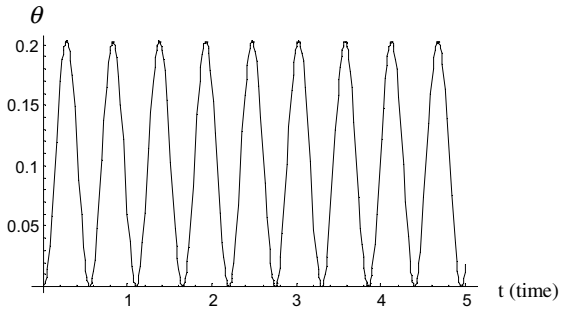

Fig. 14. Chassis angle as a function of time.

5.1. Flywheel compensation

In order to reduce or eliminate the rocking of the chassis, a moment must be applied to the chassis to counter that transmitted from the motors. One approach to creating this moment is by means of a flywheel. If the flywheel is accelerated in a direction opposite that the motor is spinning, it will create an effective moment that is opposite in direction to the motor torque. The effectiveness of the flywheel system depends on its acceleration abilities as well as the mass of the actual flywheel. The total required moment is given by Eq. (25) while its dependency on the flywheel parameters is shown by Eq. (26).

$$\frac{1}{2}M_{\mathrm{Q}} = M_{\mathrm{T}}\left(1+\frac{r_{\mathrm{m}}}{r_{\mathrm{p}}}\cos\theta_{\mathrm{p1}}\right) - \ddot{\theta}_{\mathrm{W}}\left(I_{\mathrm{p3}}\frac{r_{\mathrm{m}}}{r_{\mathrm{p}}}\left(\frac{\cos\theta_{\mathrm{p1}}+\cos\theta_{\mathrm{p2}}}{\cos\theta_{\mathrm{p3}}+\sin\theta_{\mathrm{p2}}}\right) + I_{\mathrm{p1}}\frac{r_{\mathrm{m}}}{r_{\mathrm{p}}}\cos\theta_{\mathrm{p1}} + m_{\mathrm{p1}}r_{\mathrm{m}}r_{\mathrm{W}}\right) + r_{\mathrm{m}}(2S_{\mathrm{i}}+2W_{\mathrm{i,SC}}+W_{\mathrm{i,S}})\left(\frac{\cos\theta_{\mathrm{p1}}+\cos\theta_{\mathrm{p2}}}{\cos\theta_{\mathrm{p3}}+\sin\theta_{\mathrm{p2}}}\right) + r_{\mathrm{m}}W_{\mathrm{p3}}\left(\frac{\cos\theta_{\mathrm{p1}}+\cos\theta_{\mathrm{p2}}}{\cos\theta_{\mathrm{p3}}+\sin\theta_{\mathrm{p2}}}\right) \tag{25}$$

$$M_{\mathrm{Q}} = \frac{1}{2}m_{\mathrm{FW}}(r_{\mathrm{FW}})^2\ddot{\theta}_{\mathrm{FW}} \tag{26}$$

For a typical constant-torque acceleration the required flywheel compensation acceleration is also constant. Fig. 15 shows the design tradeoffs between the total flywheel mass and the required flywheel acceleration for a typical motor acceleration. In this case the chassis is maintained vertical at all times which demonstrates that the compensation scheme can in fact improve the range of accelerations within the robot's operating envelope.

6. Impact stress analysis

The theory behind mechanical impact is still an underdeveloped field, especially with relation to complex geometries such as those of the wheels used on the robot. Therefore, in order to determine the robot's theoretical impact survivability, a combination of empirical results and engineering estimations were used to create a reasonable prediction.

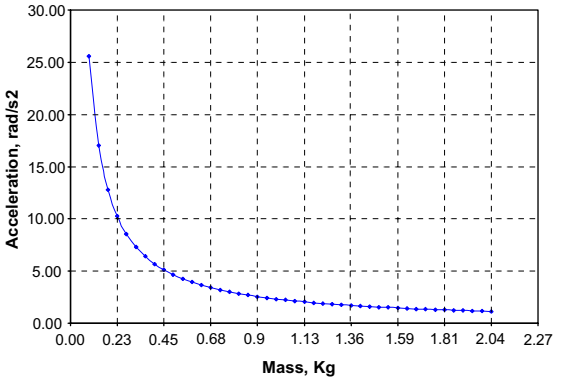

Fig. 15. Flywheel mass/acceleration trade-off.

By virtue of the design, the drive-shaft sees the greatest stress loading of any component on the robot, specifically the portion extending out from the bearings to the wheel hubs. For analysis purposes, we can essentially treat this as a cantilevered beam. Since the normal stresses developed in the shaft due to a transverse loading at the end are magnitudes greater than the shear stress, we will neglect shear stress in our calculations. If we take the yield strength of Titanium (130 ksi) as the maximum allowable, we can determine the maximum tolerable load to be 532 lbs per wheel from Eq. (27) shown below.

$$P_{\mathrm{MAX}} = \frac{\sigma_{\mathrm{MAX}}(1/4)\pi(r_{\mathrm{S}})^4}{L_1 r_{\mathrm{S}}} \tag{27}$$

The next step is to determine the corresponding maximum impact velocity. To do this we utilized the basic impulse momentum equation coupled with several empirical observations. During the experiment it was observed that the robot generally rebounded approximately 33% of the original drop height, allowing us to correlate the rebound velocity with the initial drop height by a simple kinematic equation, Eq. (28), while impact velocity is given by Eq. (29).

$$v_{\mathrm{reb}} = \sqrt{\frac{2}{3} g \cdot h_{\mathrm{drop}}} \tag{28}$$

$$v_{\mathrm{impact}} = \sqrt{2g \cdot h_{\mathrm{drop}}} \tag{29}$$

Using these relationships, we were then able to develop Eq. (30) relating drop height to maximum impulsive force using the impulse–momentum equation. Note that the time of impact (0.1 s) is estimated based on the early series of experiments. The resulting survivable height prediction is therefore 23.5 m. Given that approximations were used in arriving at this number, if we include a safety margin of 2, we still arrive at a survivable height of 11.7 m, which exceeds the desired 6.1 m survivable drop limit.

$$h_{\mathrm{drop}} = \frac{3(4-\sqrt{3})}{26g}\left(\frac{P_{\mathrm{MAX}}\Delta t}{m}\right)^2 \tag{30}$$

7. Experiments and design iterations

Three series of experiments were conducted with the robot, shown in Fig. 16, once manufacturing and assembly were complete. After the first two series, weaknesses of the robot were characterized and design improvements were formulated and implemented before beginning the next series of experiments. During the final series of trials, the robot met the original performance expectations, though further possible design improvements for the next generation will be presented.

7.1. Experiment\design iteration series 1

The first series of trials involved testing the robot's driving capabilities. The first observation from this test was that the tires were bowing inwards excessively with the chassis in certain orientations. Excessive compliance of the suspension in the lateral direction was determined to be the root cause. To rectify the problem stiffer suspension springs were installed in the two lateral positions, with custom made spacers used to maintain the static condition balance of the drive shaft.

The other major finding of the initial trials was that the drive belt was jumping off the idler pulley when the motor turned in a direction causing power transmission to first pass over the idler. While the belt would not completely fall off due to the restraining side walls of the pulley, it would come loose enough that power would not be transmitted to the drive pulley. Upon investigating this problem it was determined that the rubber belt did not have positive enough engagement with the pulleys and that the idler springs were not stiff enough, allowing the idler assembly to jump. The stiffness issue was corrected with new stiffer springs while the engagement issue called for a more drastic change. A new chain drive transmission was installed on the robot, using nylon chains which retain some of the elasticity of the rubber belt as well as not requiring lubrication.

7.2. Experiment\design iteration series 2

The second series of trials included both new driving tests as well as the first round of survivability tests. The driving tests substantiated the greatly improved positive engagement of the

Fig. 16. Assembled robot.

transmission with the new chain/sprocket system. The chains continuously remained meshed with the sprockets, unlike the belts in the previous design which tended to jump off the pulleys. As a result the new transmission yielded much more reliable and controllable driving capability.

The survivability tests were conducted as a series of drops from increasing elevations. For the very first test the robot was driven off a sidewalk ledge at a non-orthogonal angle, so that the tires left the sidewalk at different times, which in turn imparted a tumbling motion to the robot. The robot successfully righted itself and continued the driving motion, demonstrating its ability to survive a tumbling motion. The next test, which similarly tested this tumbling ability in a more drastic fashion, involved driving the robot down a flight of stairs. Again the robot survived the descent and was able to drive away successfully.

The next two tests involved drops from greater elevations. During the first of these tests, the robot was driven off a loading dock at a height of approximately 1.2 m. Again, the robot was driven off non-orthogonally resulting in an initial impact on one wheel. Subsequent observations revealed that the steel drive shaft of that wheel had undergone some plastic deformation between the spherical bearing and the hub connection, though the drive system still functioned. The next test was a manual drop from a height of 4.5 m onto concrete. During impact both shafts underwent significant plastic deformation, causing the chassis to actually partially impact the ground as well. Though the motors were still functioning and receiving power the robot no longer retained driving function. The subsequent disassembly and inspection revealed that both nylon drive chains had snapped. Several screws connecting the chassis frame elements in the area of impact had also sheared off, and the protective plates near the point of impact on the chassis had also taken some damage. The plates were easily remade and the sheared screws were extracted from the undamaged frame elements so they could be reassembled.

The transmission system, however, required a more in depth design improvement. First, new drive shafts were designed and manufactured out of titanium alloy, offering over a fourfold strength of materials improvement alone. Additionally, the portion of the shaft extending between the bearings and the hub, the portion seeing the highest stresses, was increased in diameter from 9.5 mm (3/8 in.) to 12.7 mm (1/2 in.). By keeping the inner diameter the same as before, all the prior internal components could be reused. Larger diameter tires were also installed to provide greater ground clearance, at the cost of increased weight and higher torque movement requirements. A new rubber shaft stop was also installed to reduce the unsupported motion of the shaft during impact and to increase the energy absorption of that system.

7.3. Experiment\design suggestions series 3

Once the above outlined design improvements were completed the third and final round of tests were conducted. After a quick initial retesting of the robot's driving capabilities with the improvements, a new incremental series of drop tests was begun. The drops tests included drops from heights of 1.2, 1.8, 2.4, 3, 3.7, 4.3 and finally 6.1 m (the equivalent of a third story drop) onto hardened grass covered soil. After the initial low elevation tests the drive sprocket on one of the two motors came loose. The situation was corrected by retightening and using Loctite to help secure the connection. During all subsequent tests the robot survived the drop tests without any apparent damage and was able to successful drive after the test. The robot demonstrated significant rebound during drops, shown in Figs. 17 and 18, but was able to survive all aspects of the

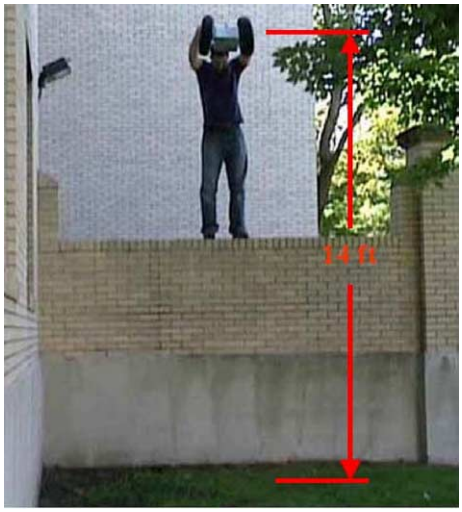

Fig. 17. Initial drop height: 4.3 m.

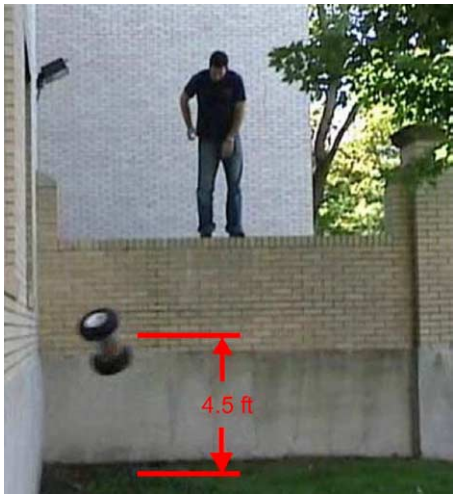

Fig. 18. Rebound height: 1.4 m.

impact event. In one scenario the robot actually rebounded into the sidewall of a building but still suffered zero damage.

Based on these final experiments it can be concluded that the basic concept of a two wheeled robot with the unique suspension system outlined within this paper can indeed succeed at surviving high impact loading, including impacts from falls of up to a third story drop as seen in Fig. 19. A number of possible design improvements were formulated at the conclusion of the tests, however, which should further enhance the robot's survivability. The primary suggestion is to replace the tires with lighter more energy absorbent wheels, such as balloon rubber tires. By reducing the

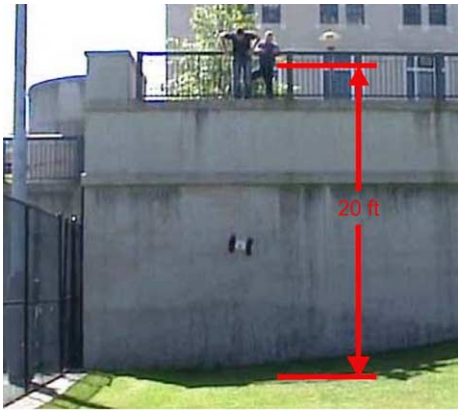

Fig. 19. Three story drop test.

weight and hence the inertia of the system, impact forces will be greatly reduced, thus allowing drops from even greater heights. Additionally, a custom rubber coupling component could be added to the external portion of the drive shaft to further improve the energy absorption of the drive system during impact loading, though care must be taken to insure sufficient rigidity of the drive shaft so that the chassis does not touch the ground during an impact event.

8. Conclusion and summary

This paper presented the development of a design for a two-wheeled mobile robot capable of withstanding high impact loading. After several rounds of testing and design iterations, the final robot utilized a chain drive transmission with a titanium drive shaft and an integrated suspension system. Previous work in creating high-impact survivable robots has emphasized building reinforced and rigid structures to withstand high energy impact loads. In contrast, our design took the approach of creating a flexible and minimilistic structure capable of absorbing the energy of impact. This design strategy makes the robot inherently less expensive to build since not as much high strength material or as many robust components are required. Experimental drop tests verified that the robot design is capable of surviving falls from at least a third story drop without any damage, thereby equaling or besting previous commercial designs of a magnitude greater cost.

References

[1] United States Fire Administration and National Fire Association. Rescue Systems I, 1993.
[2] J. Casper, M. Micire, R. Murphy, Issues in intelligent robots for search and rescue, SPIE Ground Vehicle Technology II 4 (2000) 41–46.
[3] J.M. Cameron, R.C. Arkin, Survival of falling robots, SPIE Vol. 1613 Mobile Robots VI, 1991.
[4] R.C. Arkin, Survivable robotic systems: Reactive and homeostatic control, in: M. Jamshidi (Ed.), Robotics and Remote Systems for Hazardous Environments, Prentice-Hall, 1993.
[5] Packbot, iRobot Corporation, Available from: <www.packbot.com>.

[6] Dragon Runner, CMU, National Robotics Engineering Consortium, Available from: <http://www.rec.ri.cmu.edu/projects/dragon/index.shtml>.
[7] nBot Balancing Robot, David Anderson, Available from: <http://www.geology.smu.edu/~dpa-www/robo/nbot/>.
[8] D.W. South, J.R. Mancuso, Mechanical Power Transmission Components, Marcel Dekker Inc, New York, 1994.
[9] S.S Rao, Mechanical Vibrations, Addison-Wesley Publishing Company, Reading, MA, 1995.
[10] F.P. Beer, E.R. Johnston, Vector Mechanics for Engineers: Dynamics, McGraw-Hill, New York, 1988.